ELSEVIER

J. Non-Newtonian Fluid Mech. xxx (2006) xxx–xxx

Journal of Non-Newtonian Fluid Mechanics

www.elsevier.com/locate/jnnfm

Slippage and migration in Taylor–Couette flow of a model for dilute wormlike micellar solutions

Louis F. Rossi [a,*], Gareth McKinley [b], L. Pamela Cook [a]

[a] Department of Mathematical Sciences, University of Delaware, Newark, DE 19716, USA

[b] Department of Mechanical Engineering, Massachusetts Institute of Technology, Cambridge, MA 02139, USA

Received 3 June 2005; received in revised form 8 February 2006; accepted 11 February 2006

Abstract

We explore the rheological predictions of a constitutive model developed for dilute or semi-dilute worm-like micellar solutions in an axisymmetric Taylor–Couette flow. This study is a natural continuation of earlier work on rectilinear shear flows. The model, based on a bead-spring microstructure with non-affine motion, reproduces the pronounced plateau in the stress–strain-rate flow curve that is observed in laboratory measurements of steady shearing flows. We also carry out a linear stability analysis of the computed steady-state solutions. The results show shear-banding in the form of sharp changes in velocity gradients, spatial variations in number density, and in alignment or stretching of the micelles. The velocity profiles obtained in numerical solutions show good qualitative agreement with those of laboratory experiments.

Keywords: Mathematical modeling; Inhomogeneous fluids; Dumbbell models with slippage; Worm-like micellar solutions; Taylor–Couette flow

1. Introduction

Worm-like micellar solutions are of special interest due to their extensive commercial applications and due to their unusual behavior under different flow conditions [30]. Worm-like micelles are very long cylindrical structures composed of amphiphilic surfactant molecules which self-assemble in solution. These structures are flexible and can entangle and behave much like polymers in solution, however they can also spontaneously break and reform on different time scales. Thus, they have earned the name “living polymers” [8]. Of special interest is the behavior of dilute and semi-dilute worm-like micellar solutions under shearing flow. Two characteristics observed in experiments of dilute micellar solutions have been the source of considerable experimental and theoretical investigation. First, solutions can become turbid with increasing shear rate as the result of a shear-induced phase separation (SIPS) [21,22]. Second and of more interest to the present study, the flow curve of steady shear stress versus shear-rate presents a distinct plateau [3,4]. Flow visualization of micellar solutions in this plateau region shows the formation of shear-bands [20,32,21,22,17,16]. A number of models have been proposed to explain these phenomena. In this paper, we apply a bead-spring model including a non-affine slippage term developed in Ref. [9] to describe worm-like micellar solutions in circular Taylor–Couette flows.

One of the suggested mechanisms for shear banding is that of a constitutive instability. That theory suggests that an underlying non-monotone relationship between stress and strain-rate, in steady shearing flow, is responsible for the existence of shear banded solutions. In this description, specific shear-bands consist of identical stress states on different branches of the flow curve corresponding to different strain rates. A number of studies of this behavior have focused on Johnson–Segalman-like models, that is models in which the convected derivative is a Gordon–Schowalter derivative. In early papers, studies were carried out investigating possible mechanisms for a unique choice of shear banding possibilities [11,15,26]. In order to have a model which selects unique states, higher order derivative (diffusive) terms were needed in the stress equation [27]. In conjunction with this diffusive terms were added to the constitutive relation [24,27–29]. More recently two-fluid effects and couplings between the flow and the microstructure, for example coupling between the stress and the mean micellar length, have been investigated [12–14]. Some of the most recent studies are especially relevant to experimental studies which suggest that a steady-state banding pattern is not achievable, and instead oscillatory banding patterns appear [34,14]. In particular the recent NMR study by Lopez-Gonzalez et al. [23]

* Corresponding author.
E-mail address: rossi@math.udel.edu (L.F. Rossi).

0377-0257/$ – see front matter © 2006 Published by Elsevier B.V.
doi:10.1016/j.jnnfm.2006.02.012

demonstrated a clear connection between shear-band instability and flow-microstructure coupling. In those studies mentioned above in which the Gordon–Schowalter derivative is used in the modeling, it is used phenomenologically, rather than being systematically derived from a fundamental principle or microscopic model.

In an earlier paper [9], a new model was presented for semi-dilute solutions of worm-like micellar solutions in which the non-affine motion was tracked consistently in the modeling process. Recent studies of worm-like micellar solutions have demonstrated that there can be a sequence of rheological transitions as the concentration of surfactant and counterion are progressively increased; from the dilute to the semi-dilute/entangled and ultimately to the concentrated/entangled regime. The present model is most appropriate for the semi-dilute/entangled regime in which the deformation of individual worm-like micelles (rather than network segments) is followed. The effects of chain overlap and entanglement and the continuous breaking and reforming of the worm-like micelles in the semi-dilute regime are modeled by the non-affine deformation of the microstructure. The model was derived using kinetic theory assuming that the viscoelastic characteristics of the semi-dilute solution properties could be lumped into a bead-spring mechanism. The model self-consistently incorporates "slippage/tumbling" as well as the spatial extension of the bead-spring. This work is a generalization of the Bhave et al. model for dilute polymers [5], as presented and corrected by Beris and Mavrantzas [2], to non-affine motions. In particular, the model equations form a system of partial differential equations in which the number density, velocity gradients, velocity and stress are coupled. The inclusion of "slippage/tumbling" in the model yields the Gordon–Schowalter convected derivative in the stress equation and the incorporation of spatial extension couples the stress equation with an evolution equation for the local number density of micellar chains. The latter equation is dependent on shear-rate variations, stress variations, and the slippage parameter.

Taking into account the spatial inhomogeneity of the system leads to incorporation of a spatial diffusion term in the stress equation, thus leading to the necessity of stress boundary conditions for the model. This term was included in the work of Bhave et al. [5], of El-Kareh and Leal [10] (albeit both examined affine motion), in work of Olmsted as we have pointed out earlier, and more recently in a paper of Black and Graham [7]. The most appropriate form of this boundary condition is not clear. The micelles may be modeled to select a specific alignment with the wall (a Dirichlet boundary condition) or the wall may only passively interact with the fluid (so that there is no net flux of configurations into, or out of, the wall; a Neumann boundary condition. In our work we have duplicated and explored the (Dirichlet) boundary conditions used in Ref. [5]. We have also explored the (Neumann) boundary condition as used in Black and Graham [7]and in Olmsted et.al. [28]. This diffusive term was not included in the Taylor–Couette study of Apostolakis et al. [1]. In that work, slippage is not modeled so the flow curve is monotone and diffusion is not necessary.

In the previous paper, the predictions of our model were examined in rectilinear steady-state shearing flow. It was shown, computationally, as anticipated [27] that the addition of the extra terms, especially the diffusive terms, removed the indeterminacy in the steady-state shear-banded state. Calculation of the steady-state shear stress versus shear-rate curve for this model shows that the shear stress first increases with shear rate, then plateaus, and only rises again at much higher shear rates. Thus, the viscosity as a function of shear rate first decreases slowly (slight shear thinning) as the shear-rate increases, then drops quickly proportional to $\dot{\gamma}^{-1}$ and then, at much higher shear rates, levels off to its asymptotic solvent limit.

The inclusion of slippage/tumbling effects incorporates a non-affine motion into the model [19]. This non-affine motion is consistent with breakage and re-formation of the worm-like micelles under an imposed shearing deformation. The measure of the non-affine motion is $\xi = 1 - a$. When $a = 1$, $\xi = 0$, the motion is affine. As a decreases from 1, the motion becomes more strongly non-affine. Shear banding behavior and the concurrent stress plateau can only occur if the underlying flow curve is nonmonotone, that is if $\xi \neq 0$, or more precisely if $|a| < 1$ and $\beta < n_0 a^2/8$, where n_0 is the number density and $\beta = \eta_s/\eta_0$ is the solvent viscosity ratio (see Section 3).

The generic trends observed in the flow curve discussed above are typical of results of experimental measurements of worm-like micellar solutions which exhibit shear banding and turbidity [17,21]. The shear banding behavior and increasing turbidity occur in the intermediate shear-rate region when the stress plateaus. In the rectilinear shear situation, shear banding does occur for this model, albeit in a very small interval of shear-rates. The shear banding behavior is characterized by a velocity profile that quickly falls from the wall value through a boundary layer, then levels off, then falls rapidly again through an internal shear layer to a lower velocity through the middle of the gap, before rising symmetrically on the other side. For the rectilinear shear case no number density layers were seen for this model other than the depletion layers at the wall [9]. This situation may be considerably different in the case of a torsional shear flow such as a cone-plate or Taylor–Couette flow, due to the effects of spatial curvature. Experiments definitely suggest [32,21,17] that shear layers first form near the inner wall where the curvature is highest.

In this paper, we examine the non-affine model developed in the previous paper, but in a circular Taylor–Couette flow. We compare the predictions with those available from experiments on micellar solutions [17,20,21,32]. The geometry we study consists of two concentric cylinders with an inner cylinder of radius R_1, an outer cylinder of radius R_2 and a gap width of $H = R_2 - R_1$. The inner cylinder is held fixed while the outer cylinder rotates at velocity $\tilde{v}|_w$. We compute the flow curve and study the linear stability of steady-state solutions to 1D perturbations under shear-rate controlled conditions, in which the outer cylinder velocity is fixed, and under stress-controlled boundary conditions. Calculations show the formation of shear banding structures manifested both as sudden changes in the velocity gradient and as number density fluctuations. Results from the model are compared with experimental results for a micellar solution (surfactant system of 6% cetylpyridium chloride and 1.4% sodium salicylate (2:1 molar ratio) dissolved in 0.5 M NaCl brine [17]).

2. Model

The physical variables involved in the analysis are denoted with a $\tilde{()}$ and are non-dimensionalized as follows: $r = \frac{\tilde{r}}{H}$, $t = \frac{\tilde{t}}{\lambda}$, $\mathbf{v} = \frac{\lambda \tilde{\mathbf{v}}}{H}$, $\boldsymbol{\tau} = \frac{\tilde{\boldsymbol{\tau}}}{n_{\mathrm{av}} kT}$, $n = \frac{\tilde{n}}{n_{\mathrm{av}}}$, where H is the gap width, k the Boltzmann constant, T the temperature, and n_{av} is the average number density of micelles $n_{\mathrm{av}} = \int_{R_1}^{R_2} \tilde{r}\tilde{n}(\tilde{r})\,\mathrm{d}\tilde{r}$.

Note that the typical velocity scale is based on the gap width and relaxation time. This non-dimensionalization results in two non-dimensional parameters for a given $v|_{\mathrm{w}}$; namely the Deborah number $De = \frac{\lambda \tilde{v}|_{\mathrm{w}}}{H}$, the ratio of the relaxation time λ to the typical fluid flow time, and the Peclet number $Pe = \frac{H\tilde{v}|_{\mathrm{w}}}{D_{\mathrm{tr}}}$, where D_{tr} is the translational diffusivity of the micelles. With this scaling both shear-rate controlled and stress-controlled cases can be examined easily through changes in boundary conditions only. The ratio of De to Pe, $\epsilon = \frac{De}{Pe} = \frac{\lambda D_{\mathrm{tr}}}{H^2}$, is typically small [5]. The parameter $\xi = 1 - a$ measures the extent of non-affineness in the model, $\beta = \frac{\eta_{\mathrm{s}}}{\eta_{\mathrm{p}}}$ measures the solvent viscosity relative to the average "polymer" (micellar contribution to the) viscosity, $\eta_{\mathrm{p}} = n_{\mathrm{ave}} kT\lambda$. The Reynolds number for the flow is typically small, hence only inertialess flows are considered. Notation conventions are as in Ref. [6].

The dimensionless governing equations for the fluid flow are as follows. Conservation of mass:

$$\nabla \cdot \mathbf{v} = 0. \tag{1}$$

Conservation of momentum (inertialess flow):

$$\nabla \cdot \Pi = 0, \tag{2}$$

where

$$\Pi = p\boldsymbol{\delta} - \beta\dot{\boldsymbol{\gamma}} + \boldsymbol{\tau}_{\mathrm{p}} \tag{3}$$

is the total stress. Here $\dot{\boldsymbol{\gamma}} = \nabla\mathbf{v} + (\nabla\mathbf{v})^t$. The dimensionless number density n and deviatoric stress $\boldsymbol{\tau}_{\mathrm{p}}$ are given by

$$a\frac{Dn}{Dt} = \epsilon(a\nabla^2 n + \nabla\nabla : \boldsymbol{\tau}_{\mathrm{p}} + \xi\nabla\nabla : ((\boldsymbol{\tau}_{\mathrm{p}} - an\boldsymbol{\delta}) \cdot \dot{\boldsymbol{\gamma}})), \tag{4a}$$

$$\boldsymbol{\tau}_{\mathrm{p}} + \boldsymbol{\tau}_{\mathrm{p}(\diamond)} - \epsilon\nabla^2\boldsymbol{\tau}_{\mathrm{p}} - \left(a\frac{Dn}{Dt} - \epsilon a\nabla^2 n\right)\boldsymbol{\delta} = -a^2 n\dot{\boldsymbol{\gamma}}. \tag{4b}$$

Here $()_{(\diamond)}$ represents the Gordon–Schowalter derivative:

$$()_{(\diamond)} = \frac{D()}{Dt} - (\nabla\mathbf{v})^t \cdot () - () \cdot \nabla\mathbf{v} + \frac{\xi}{2(\dot{\boldsymbol{\gamma}} \cdot \boldsymbol{\tau}_{\mathrm{p}} + \boldsymbol{\tau}_{\mathrm{p}} \cdot \dot{\boldsymbol{\gamma}})}, \tag{5}$$

and

$$\boldsymbol{\tau}_{\mathrm{p}} = an\boldsymbol{\delta} - \frac{aH_{\mathrm{s}}}{n_{\mathrm{av}}kT}\{\mathbf{QQ}\}, \tag{6}$$

where H_{s} is the Hookean spring force, $\mathbf{Q}$ is the connector vector between the two beads (from bead 1 to bead 2) in the bead-spring, and $\{\}$ signifies the ensemble average distribution. That is $\{\mathbf{QQ}\} = \sum_\nu \int \mathbf{QQ}\Psi_{\mathrm{p}}\,\mathrm{d}\mathbf{Q}$ where $\Psi_{\mathrm{p}}(\tilde{r} - (-1)^\nu\mathbf{Q}/2, \mathbf{Q}, t)$ and $n = \sum_\nu \int \Psi\,\mathrm{d}\mathbf{Q}$ (see Refs. [5,9]), where the sum is over the two beads $\nu = 1$ and 2. Note that in the affine limit this model agrees with the essential elements of several models derived by different means; see Beris and Mavrantzas [2].

The boundary conditions for the problem are as in Refs. [9,5]:

(1) No flux of micelles through the boundaries:

$$\hat{\mathbf{n}} \cdot \mathbf{j}_{\mathrm{p}} = \hat{\mathbf{n}} \cdot a\nabla n + \nabla \cdot \tau_{\mathrm{p}} + \xi\nabla \cdot [(\boldsymbol{\tau}_{\mathrm{p}} - an\boldsymbol{\delta}) \cdot \dot{\boldsymbol{\gamma}}] = 0. \tag{7}$$

(2) Conservation of the total number of micelles:

$$\int_\Omega \int ndA = \pi(r_0^2 - r_i^2). \tag{8}$$

(3) Either; alignment of the molecules at the wall:

$$\boldsymbol{\tau}_{\mathrm{pw}} = an_{\mathrm{w}}\left(\boldsymbol{\delta} - \frac{H_{\mathrm{s}}\{Q^2\}_{\mathrm{w}}}{kT\tilde{n}_{\mathrm{w}}}(\hat{\mathbf{t}}\hat{\mathbf{t}})\right). \tag{9a}$$

Here $\tilde{n}_{\mathrm{w}} = n_{\mathrm{av}}n_{\mathrm{w}}$ is the dimensional number density at the wall, and $\hat{\mathbf{t}}$ is a unit tangent to the wall. Since flows considered in this paper will have no z dependence, $\hat{\mathbf{t}}$ is the unit tangent vector in the flow direction. Future work will examine three dimensional effects and thus will examine the effect of alignment of the micelles along the wall, but not necessarily solely in the flow direction; or, no flux of the conformation across the wall:

$$\hat{\mathbf{n}} \cdot \nabla\{\mathbf{QQ}\} = 0, \tag{9b}$$

where $\hat{\mathbf{n}}$ is the unit normal to the wall. Further discussion of these boundary conditions is given below.

(4) Specification of either the velocity v (shear-rate controlled) or the stress $\boldsymbol{\tau} \cdot \hat{\boldsymbol{t}}$ (stress-controlled) at the solid walls.

In this paper, we focus on the computation of steady solutions and their stability. Future work will examine time evolution of the flows from rest, dependence on initial state, and further investigate boundary conditions at the wall.

3. Axisymmetric Taylor–Couettev flow

We consider axisymmetric solutions to the system (1)–(19) for which the velocity has the form $u_r = 0$, $u_\theta = v(r)$, $u_z = 0$. Here the subscripts indicate the component, and no variations in the θ or z directions are considered. Mass is automatically conserved and the components of the momentum Eq. (2) reduce to

$$\frac{1}{r^2}\frac{\partial}{\partial r}\left(r^2\left[\tau_{pr\theta} - \beta r\frac{\partial}{\partial r}\left(\frac{v}{r}\right)\right]\right) = 0, \tag{10a}$$

where $\beta = \eta_{\mathrm{s}}/\eta_{\mathrm{p}}$ as defined earlier:

$$\frac{1}{r}\frac{\partial}{\partial r}(r\tau_{prr}) - \frac{\tau_{p\theta\theta}}{r} + \frac{\partial p}{\partial r} = 0. \tag{10b}$$

The equations for the number density (4a) and extra stress components (4b) reduce to:

$$a\frac{\partial}{\partial t}n - \epsilon\left(a\frac{1}{r}\frac{\partial}{\partial r}\left(r\frac{\partial n}{\partial r}\right) + \frac{1}{r}\frac{\partial^2}{\partial r^2}(r\tau_{prr}) - \frac{1}{r}\frac{\partial}{\partial r}\tau_{p\theta\theta}\right.$$
$$\left. + \xi\left[\frac{1}{r}\frac{\partial}{\partial r}\left\{r\frac{\partial}{\partial r}\left[\tau_{pr\theta}\left(r\frac{\partial}{\partial r}\left(\frac{v}{r}\right)\right)\right]\right\}\right]\right) = 0, \tag{10c}$$

$$\begin{aligned}&\frac{\partial}{\partial t}\tau_{p\theta\theta} + \tau_{p\theta\theta} - 2\tau_{pr\theta} r\frac{\partial}{\partial r}\left(\frac{v}{r}\right) + \xi\tau_{pr\theta} r\frac{\partial}{\partial r}\left(\frac{v}{r}\right)\\ &\quad - \epsilon\left[\frac{1}{r}\frac{\partial}{\partial r}\left(r\frac{\partial}{\partial r}\tau_{p\theta\theta}\right) + \frac{2}{r^2}\left(\tau_{prr} - \tau_{p\theta\theta}\right)\right]\\ &\quad - \epsilon\left(\frac{1}{r}\frac{\partial^2}{\partial r^2}(r\tau_{prr}) - \frac{1}{r}\frac{\partial}{\partial r}\tau_{p\theta\theta}\right.\\ &\quad \left. + \xi\left[\frac{1}{r}\frac{\partial}{\partial r}\left\{r\frac{\partial}{\partial r}\left[\tau_{pr\theta}\left(r\frac{\partial}{\partial r}\left(\frac{v}{r}\right)\right)\right]\right\}\right]\right) = 0,\end{aligned} \tag{10d}$$

and

$$\begin{aligned}&\frac{\partial}{\partial t}\tau_{pr\theta} + \tau_{pr\theta} - \tau_{prr} r\frac{\partial}{\partial r}\left(\frac{v}{r}\right) + \frac{\xi}{2} r\frac{\partial}{\partial r}\left(\frac{v}{r}\right)(\tau_{prr} + \tau_{p\theta\theta})\\ &\quad - \epsilon\left(\frac{1}{r}\frac{\partial}{\partial r}\left(r\frac{\partial}{\partial r}\tau_{pr\theta}\right) - \frac{4}{r^2}\tau_{pr\theta}\right) = -a^2 nr\frac{\partial}{\partial r}\left(\frac{v}{r}\right),\end{aligned} \tag{10e}$$

$$\begin{aligned}&\frac{\partial}{\partial t}\tau_{prr} + \tau_{prr} + \xi r\frac{\partial}{\partial r}\left(\frac{v}{r}\right)\tau_{pr\theta}\\ &\quad - \epsilon\left(\frac{1}{r}\frac{\partial}{\partial r} r\frac{\partial}{\partial r}\tau_{prr} - \frac{2}{r^2}(\tau_{prr} - \tau_{p\theta\theta})\right)\\ &\quad - \epsilon\left(\frac{1}{r}\frac{\partial^2}{\partial r^2}(r\tau_{prr}) - \frac{1}{r}\frac{\partial}{\partial r}\tau_{p\theta\theta}\right.\\ &\quad \left. + \xi\left[\frac{1}{r}\frac{\partial}{\partial r}\left\{r\frac{\partial}{\partial r}\left[\tau_{pr\theta}\left(r\frac{\partial}{\partial r}\left(\frac{v}{r}\right)\right)\right]\right\}\right]\right) = 0.\end{aligned} \tag{10f}$$

The boundary conditions at the walls ($r = r_1 = \frac{R_1}{H}$, $r = r_2 = \frac{R_2}{H}$) are that there is no flux:

$$a\frac{\partial n}{\partial r} + \frac{1}{r}\frac{\partial}{\partial r}(r\tau_{prr}) - \frac{\tau_{p\theta\theta}}{r} + \xi\left\{\frac{\partial}{\partial r}\left(\tau_{r\theta} r\frac{\partial}{\partial r}\left(\frac{v}{r}\right)\right)\right\} = 0,$$

and either we specify the stress components at the wall:

$$\begin{aligned}&\tau_{prr|\mathrm{w}} = an_{\mathrm{w}},\\ &\tau_{pr\theta|\mathrm{w}} = 0,\\ &\tau_{p\theta\theta|\mathrm{w}} = an_{\mathrm{w}}\left\{1 - \frac{H_{\mathrm{s}}}{kT}\frac{\{\mathbf{QQ}\}_{\theta\theta|\mathrm{w}}}{\tilde{n}_{\mathrm{w}}}\right\} = an_{\mathrm{w}}(1-d),\end{aligned} \tag{11a}$$

or we specify the normal derivative of the conformation

$$\frac{\partial}{\partial r}\{\mathbf{QQ}\}|_{\mathrm{w}} = 0. \tag{11b}$$

Here d is a measure of the number of dumbbells and their extension of the springs at the wall in the flow direction, and $\tilde{n}_{\mathrm{w}} = n_{\mathrm{w}} n_{\mathrm{av}}$ is the dimensional value of the number density at the wall. We also specify either shear-rate controlled boundaries in which the velocity $v|_{\mathrm{w}}$ is specified at both walls, or stress-controlled boundary conditions ($v = 0$ specified at one wall and stress specified on the other). Finally, the dimensionless number density must be conserved:

$$\int_{r_1}^{r_1+1} rn\,\mathrm{d}r = \frac{1}{2}[(r_1+1)^2 - r_1^2] = r_1 + \frac{1}{2}.$$

The problem outlined above is a singular perturbation problem in ϵ. For this problem ϵ is small. If $\epsilon = 0$ then there are no spatial derivatives of the stress left in the model, and the stress boundary conditions can not be satisfied. One expects, therefore, that the solution consists of pieces of an "outer" solution joined by boundary layers in which the solution variables (including the velocity field and number density) vary rapidly. In the "outer" regions the stress derivatives are order 1, in the boundary/shear layers the stress derivatives are order $\frac{1}{\epsilon^{1/2}}$. The lowest order outer stress for $\epsilon = 0$ is the solution to the Johnson–Segalman equation:

$$\tau_{pr\theta}^{(0)} = \frac{-a^2\dot{\gamma}^{(0)}}{1 + (1-a^2)(\dot{\gamma}^{(0)})^2}, \tag{12}$$

$$N_1^{(0)} = \tau_{prr}^{(0)} - \tau_{p\theta\theta}^{(0)} = \frac{2a^2(\dot{\gamma}^{(0)})^2}{1 + (1-a^2)(\dot{\gamma}^{(0)})^2}, \tag{13}$$

and also $n^{(0)} = 1$. Here $\dot{\gamma}^{(0)} = r(\frac{v_0}{r})'$ is one of the roots of (12). Note that the non-dimensional value of shear rate $\dot{\gamma}^{(0)}$ is related to the dimensional value as in Section 2:

$$\dot{\gamma}^{(0)} = \tilde{r}\lambda\frac{\partial}{\partial\tilde{r}}\left(\frac{\tilde{v}}{\tilde{r}}\right) = \lambda\tilde{\dot{\gamma}}^{(0)}. \tag{14}$$

The determination of which root should be selected can be made through matching with the shear/boundary layers. Notice that for a fixed value of a, $N_1^{(0)}$ increases with $\dot{\gamma}^{(0)}$ up to a maximum plateau value of $\frac{2a^2}{1-a^2}$ for $a < 1$. Thus the maximum value of the first normal stress difference increases as a gets closer to 1. If a is identically 1 then the shear stress is monotone as a function of shear rate, and $N_1^{(0)}$ increases, as $(\dot{\gamma}^{(0)})^2$, without bound.

4. Calculations and results

We calculate steady solutions to the system of Eq. (10) to explore general flow characteristics for comparison with similar laboratory experiments, and we also calculate the steady flow curve to confirm the existence of a plateau in the stress/shear-rate relationship. The non-dimensional geometric and parameter values are shown in Table 1. The non-dimensionalized geometry of our flow calculations are similar to the geometries of [17,32,21]. The value of ϵ was suggested by Rothstein [31]. The results are presented in terms of the dimensionless gap variable $y = \frac{\tilde{r}-R_1}{H}$. The ratio of viscosities, β is the same as that used in Ref. [5]. Most calculations were carried out with $a = 0.8$. However, we present results for $a = 0.9$ and 1 where necessary to show parameter sensitivities. Note that for $a = 1$ the motion is affine. The choice of specifying Dirichlet conditions on the stress at the wall, that is the alignment of the micelles at the walls, follows the choice of Ref. [5] and the analysis of Ref. [25]. In fact in Ref. [25] the conformation tensor $\boldsymbol{C}$ is decomposed as $\boldsymbol{C} = n\boldsymbol{c}$, where $\boldsymbol{c}$ is a single molecule or specific configuration tensor. Mavrantzas and Beris found that not only does $\boldsymbol{c}$ align parallel to the wall, but that also $n_{\mathrm{w}} = 0$. In our formalism n is allowed to adjust itself at the wall. The choice of d, that is the projection of the scaled second moment in the wall direction at the wall, needs more investigation. As will be seen, in the range $0 \leq d \leq 1$ the model predictions are relatively insensitive to d. Note that for this model, the quantity $\{\mathbf{QQ}\}$ is a weighted ensemble average of the molecular length which intrinsically involves the number density. The alternative choice of specifying

Table 1
Flow geometry and fluid solution parameters for the calculations presented in this paper

Parameter	Value
r_1	15
v_1	0
v_2	De
ϵ	10^{-3}
ξ or $1-a$	0.2
d	1/8
β	2.41×10^{-2}

All values are dimensionless.

no conformation flux at the wall, a Neumann condition on the stress, follows the choice of Black and Graham [7]. It is interesting that in this case the values of d, the dimensionless micellar alignment at the wall, selected by the model are not the same at the inner and outer wall, at least along the plateau region of the flow curve.

The numerical techniques used for these calculations are very similar to those used in Refs. [9,18,33]. We solve the boundary value problem with either shear-rate or stress controlled boundary conditions using fourth order spatial collocation where the number density at the inner cylinder wall, $n(r_1)$, is specified. Thus, the integral $\int_{r_1}^{r_1+1} n(r)r\,\mathrm{d}r$ is now a function of a single variable which is the number density at the inner wall $n(r_1)$. Thus, the number density constraint reduces to finding the root:

$$\int_{r_1}^{r_1+1} n(r)r\,\mathrm{d}r - r_1 - \frac{1}{2}$$

as a function of $n(r_1)$. We find that secant iterations work well. "Adams family" continuation methods are used to calculate solutions along the flow curve $\tau_{r\theta}(\dot{\gamma})$. The choice of shear-rate controlled or stress-controlled boundary conditions is not important except where the flow curve is close to horizontal (vertical) at which time it is necessary to use shear-rate (stress) controlled boundary conditions to continue solutions along the flow curve. For instance, when the flow curve is close to horizontal, the solution is very sensitive to stress-controlled boundary conditions, but one can converge rapidly to a solution by specifying the shear rate.

4.1. Dirichlet stress boundary condition computations

To construct the flow curve for the Dirichlet conditions (stress specified at the wall), we calculate steady solutions for a typical Couette cell geometry and typical flow parameters as shown in Table 1. In Fig. 1, we see that the new model produces a flow curve with a distinct plateau. The vertical axis represents the total shear stress:

$$\tau_{r\theta} = \tau_{pr\theta} - \beta r\left(\frac{v}{r}\right)',$$

measured at the outer wall $r = R_2$. (Hereafter $()'$ represents $\frac{\mathrm{d}}{\mathrm{d}r}$ or $\frac{\partial}{\partial r}$ as the case may be.) The horizontal axis is the dimensionless apparent shear rate $De = \lambda v/H$. Notice that in Fig. 1(a) for a small range of shear rates ($10 < De < 12.5$) there are two possible stable shear-rate controlled solutions. This non-uniqueness does not occur in the stress-controlled case shown in Fig. 1(b). As we see in Fig. 2, the local velocity gradient of $\frac{\partial v_\theta}{\partial y}$ is not uniform across the gap. Hence, we plot the spatial variations in the velocity profile for various apparent shear rates. Along the flow curve, as we increase the Deborah number up to the plateau values of stress, a boundary layer in the velocity field forms at the inner cylinder. The velocity field in the high shear band that develops at the inner cylinder exhibits a linear profile, and grows into the gap as the apparent shear-rate increases. As De is increased from 2.5 to 10, the total stress remains constant, that is the flow curve corresponding to the imposed stress/strain-rate has a plateau. The width of the high shear-rate band, starting from the inner cylinder, grows as the apparent shear-rate increases. A modest boundary layer also forms at the outer cylinder to attain the correct outer cylinder velocity. The computed velocity profile shows a two banded structure with one sharp transition region (and a third boundary layer near the outer wall as shown in Fig. 2a, the width of which goes to zero as ϵ goes to zero) similar to those profiles measured by Hu and Lips [17], Liber-

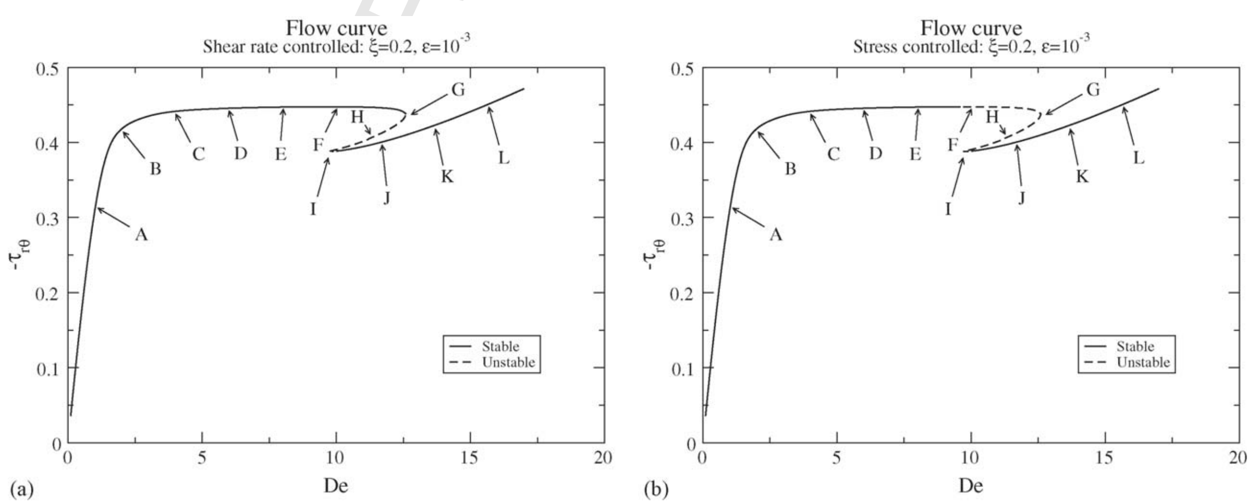

Fig. 1. Flow curves using parameters provided in Table 1. Regions of stability are indicated with either shear-rate controlled boundary conditions (a) or stress-controlled boundary conditions (b). The total stress is measured at the outer wall. (With orientation and wall stress specified.)

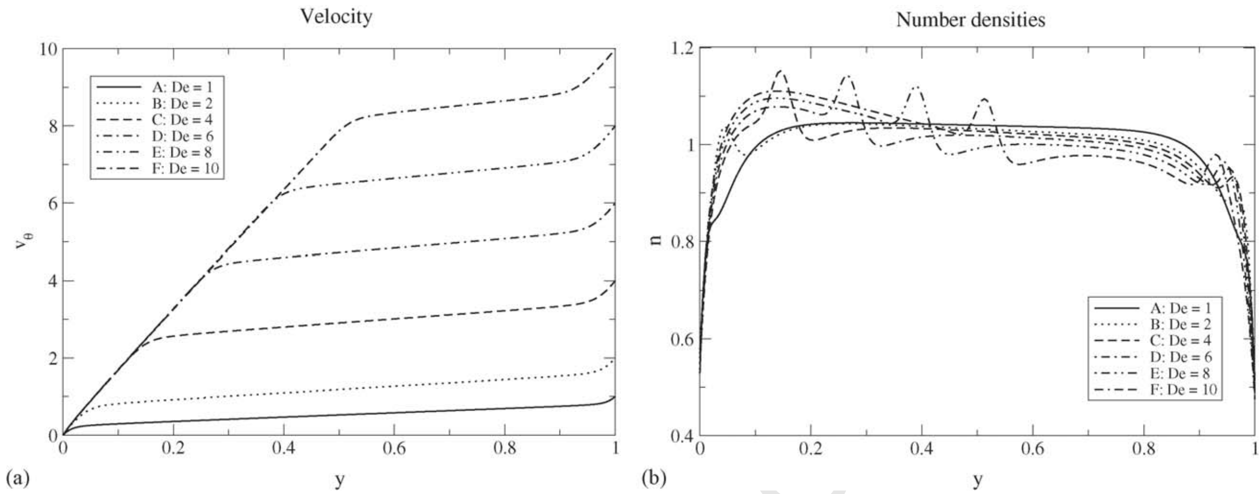

Fig. 2. Flow velocity and number densities along the left stable branch of the flow curve at positions A–F. (Wall stress specified.) Solutions at point F are linearly unstable when stress-controlled boundary conditions are applied at the outer wall.

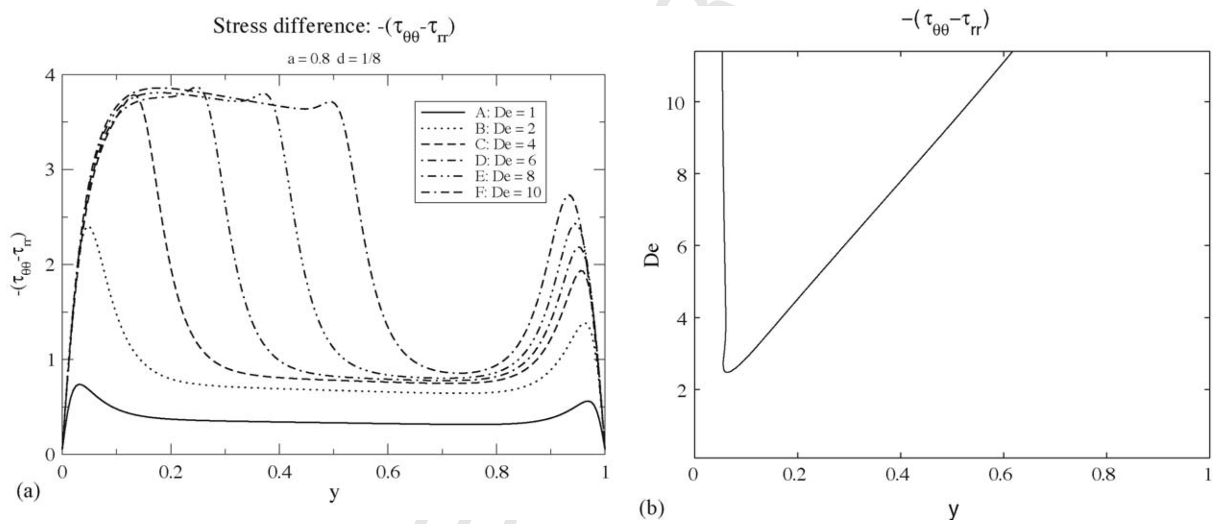

Fig. 3. In (a), radial variations in the first normal stress difference are plotted against the apparent shear rate. At right, (b) we show the spatial extent of first normal stress difference contour for $N_1 = 3$ as Deborah number is increased (wall stress specified). Solutions at point F are linearly unstable when stress-controlled boundary conditions are applied at the outer wall.

atore et al. [21] and Salmon et al. [32] in Couette geometries, although the latter profiles do not exhibit the boundary layer at the outer cylinder. In the latter two cases, the outer cylinder remains stationary whilst the inner rotates.

As observed in our study of rectilinear flow there is a depletion in the local concentration of micelles near the wall. However, in this cylindrical geometry, two distinct local maxima or number density bands form, one near the inner and one near the outer cylinder walls. In Fig. 2, we see that the inner aggregation layer of micelles moves into the gap as the shear-rate increases. The much smaller local maxima near the outer wall remains roughly unchanged as the shear-rate grows and this is a consequence solely of the no flux/no penetration boundary condition. By contrast, the notable local maximum in concentration toward the inner wall occurs in the region where the velocity gradient changes sharply. This local change in fluid density may well be connected to the onset of turbidity that is observed experimentally [4].

To understand the alignment and stretching of the molecules, we examine the first normal stress difference:

$$N_1 = -(\tau_{p\theta\theta} - \tau_{prr}) = \frac{aH_s}{n_{av}kT}(\{\mathbf{QQ}\}_{\theta\theta} - \{\mathbf{QQ}\}_{rr}). \tag{15}$$

At the wall, the first normal stress difference is specified to be a small but nonzero value, see (11a):

$$N_1 = -(\tau_{p\theta\theta} - \tau_{prr})|_w = \frac{aH_s}{n_{av}kT}\{\mathbf{QQ}\}_{\theta\theta} = an_w d. \tag{16}$$

In Fig. 3, we see that a region with strong molecular alignment or stretching originates near the inner cylinder and grows into the gap as the apparent shear-rate grows. This alignment reaches a maximum value for large enough shear rates, $De \gtrsim 4$,

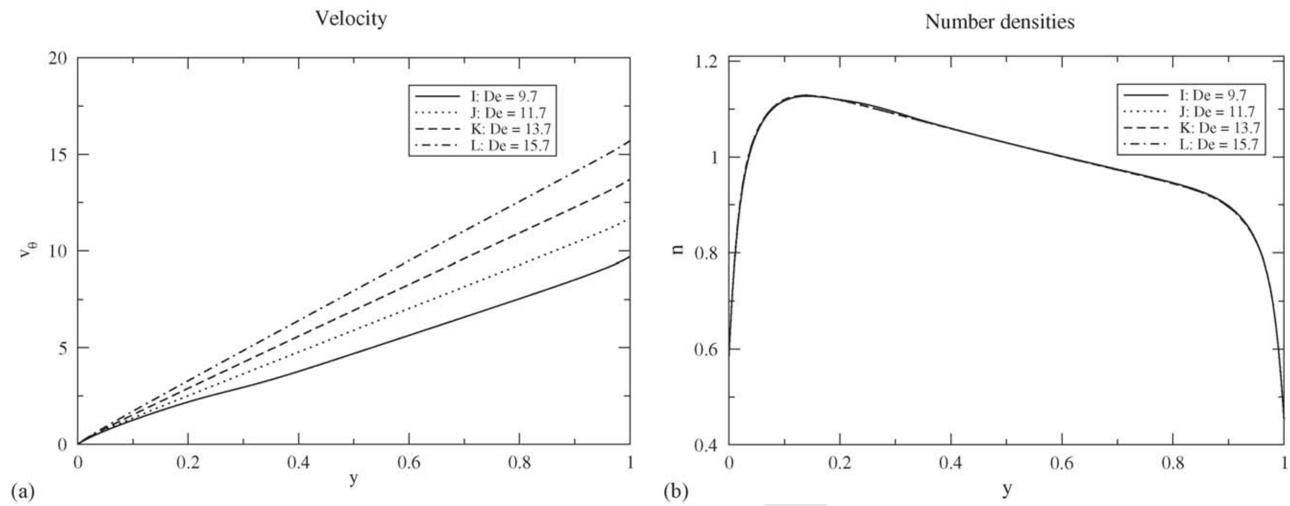

Fig. 4. Flow velocity and number densities along the right stable branch of the flow curve at positions I–L. The number density curves superpose one another. (Wall stress specified.)

and the maximum is subsequently independent of De. The value of this maximum depends only on a as predicted by the outer solution (12) for large $\dot{\gamma}^{(0)}$ and as discussed in the next paragraph. The sharp downward transition in the first normal stress difference that signifies the end of the aligned/stretched region is associated with the local maximum in number density (see Fig. 2 for comparison). In experiments, the shear-induced phase transitions that develop as the shear rate is steadily increased are associated with strong local stretching and concomitant increases in the turbidity or local number density [23] that are reminiscent of those predicted by the present model. Fig. 3(a) shows the growth of the alignment/stretched region across the gap. Fig. 3(b) follows the steady propagation of the $N_1 = 3$ contour across the gap as the De number increases. Although we have chosen this contour arbitrarily this criterion may represent – at least qualitatively – a suitable condition for the onset of a shear-induced structural transition beyond a critical degree of stretching that results in sample turbidity. Note that this high-stress turbidity-prone region is not at the wall, but is located close to the inner surface and expands into the gap as the shear-rate increases. This is also consistent with birefringence experiments [20,22].

Continuing along the flow curve past the plateau, the right hand (stable) branch exhibits solutions with flow profiles that are close to Newtonian, and the number density distribution remains unchanged with increasing De (as shown in Fig. 4).

To examine the sensitivity of the first normal stress difference to variations in constitutive parameters, we varied the parameters a and d. Calculations show that there are no changes in the first normal stress difference across the gap as d is varied between 0 and 1. The model predictions are insensitive to variations in d in this range. Note from (11) that the boundary conditions assume that the micelles are aligned at the wall ($\{\mathbf{QQ}\}_{rr} = 0$) and d measures the scaled extension of the micelles along the wall. The results are thus insensitive to this parameter at least in the range $0 \leq d \lesssim 1$. Fig. 5 shows a comparison of the first normal stress difference with variations in a. It is particularly interesting to note the extreme sensitivity of the model to changes in a. When

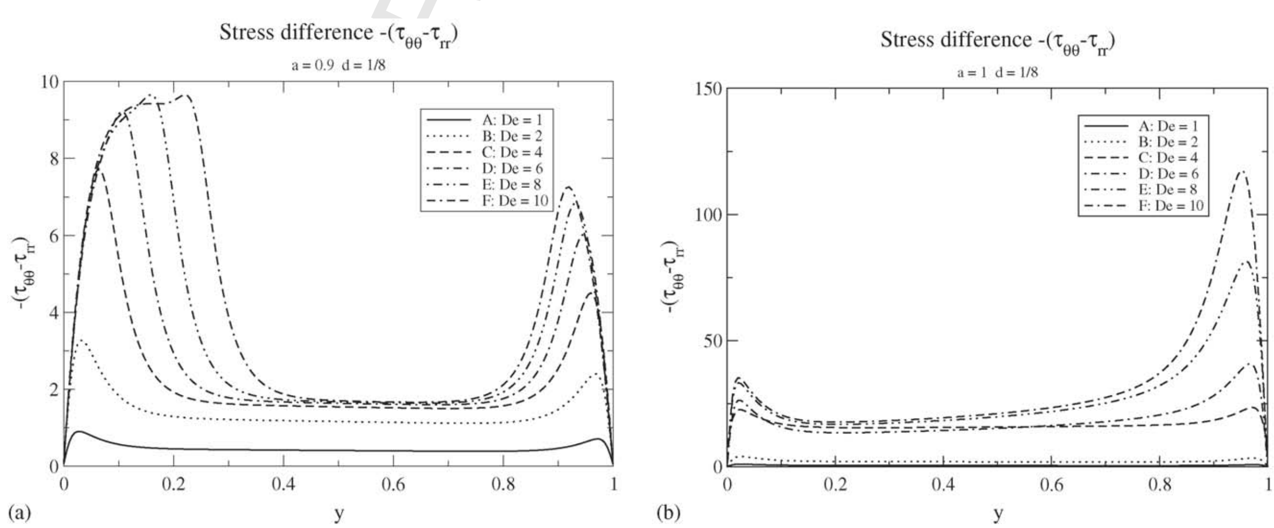

Fig. 5. First normal stress difference for $a = 0.9$ (a) and $a = 1$ (b). These should be compared with Fig. 3 (a) where $a = 0.8$. (Wall stress specified.)

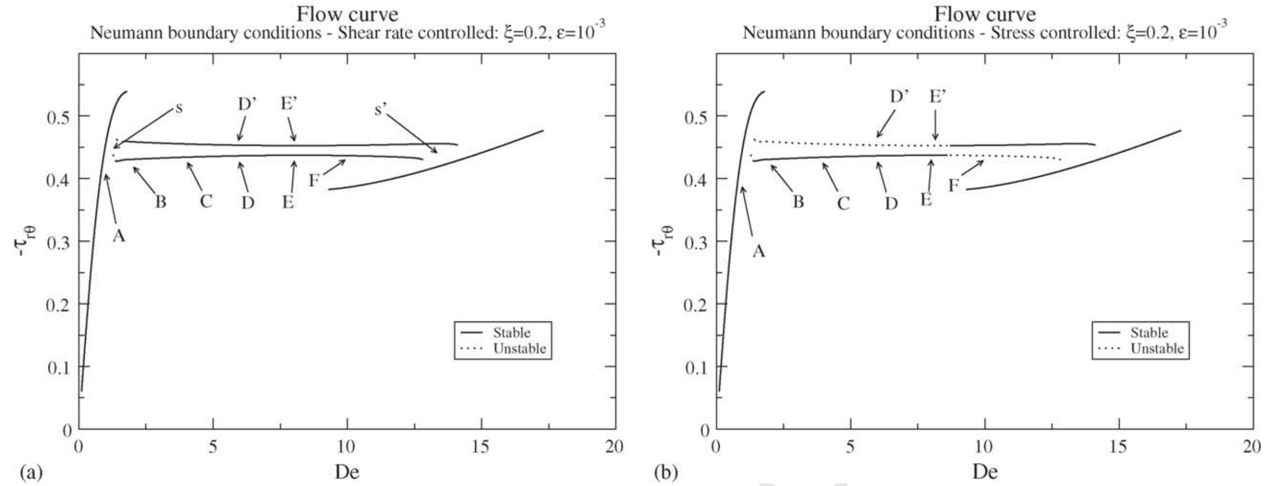

Fig. 6. A flow curve using parameters provided in Table 1 analogous to Fig. 1 but using Neumann stress boundary conditions on the conformation tensor {**QQ**}.

$a=1$ the underlying flow curve is monotone and the model reduces to the (corrected) Bhave et al. model. The first normal stress difference has a large maximum near, but not at, the outer wall for $a=1$. As a decreases, a maximum in N_1 develops near, but not at, the inner wall, and the location at which this maximum is obtained propagates into the gap as De increases. As a decreases the magnitude of this maximum decreases, but the growth of the region of maximum first normal stress propagates more quickly into the interior. Since calculations show that the radial variation in the number density $n(r)$ does not vary appreciably with a (certainly not as strongly as N_1), the increase of the first normal stress is primarily due to an increase in either the number of molecules aligned in the flow direction and/or the length of these molecules. Note that the plateau values of N_1 agree with the values of N_1 predicted for the outer ($\epsilon=0$) (Johnson–Segalman) solution for large $\dot{\gamma}$ (see (13)). That prediction, for homogeneous flows, was that for large $\dot{\gamma}$, $N_1 \sim \frac{2a^2}{1-a^2}$. Note that this value, the asymptote of the zeroth order solution and the maximum observed in the full inhomogeneous numerical calculations, is independent of $\dot{\gamma}$.

4.2. Computations with Neumann conformation boundary conditions

To construct the flow curve for the Neumann conditions (normal derivative of the conformation tensor specified at the wall) we again use the parameters of Table 1. Since we specify the stress normal derivatives, d is computed rather than imposed on the system, and we shall see later that d_{i} and d_{o}, values of d at the inner/outer wall, respectively, differ in some regions of the flow curve. The flow curve for the shear-rate controlled case is shown in Fig. 6(a) and for the stress-controlled case in Fig. 6(b). These flow curves differ from those obtained with the Dirichlet stress condition case (Fig. 1) in two ways. First, the Neumann curves have a peak located at $De=1.2$, $\tau_{r\theta}=-0.54$. Second, these curves have two stable branches in the "plateau" region.

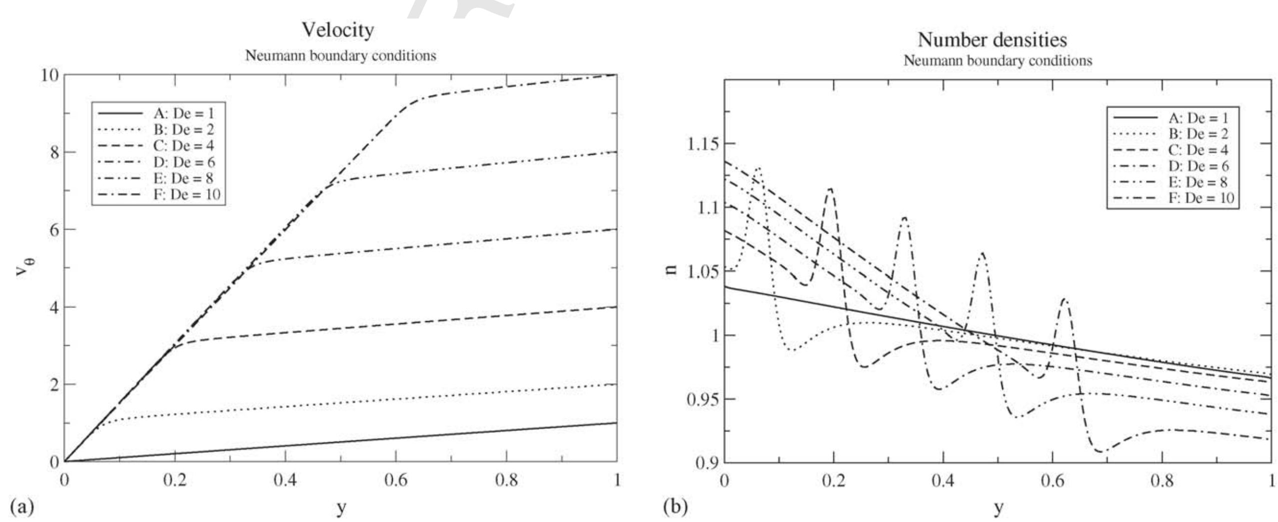

Fig. 7. Flow velocity and number densities along the left stable branch of the flow curve at positions A–F following the lower plateau as indicated in Fig. 6 with Neumann boundary conditions on the conformation tensor.

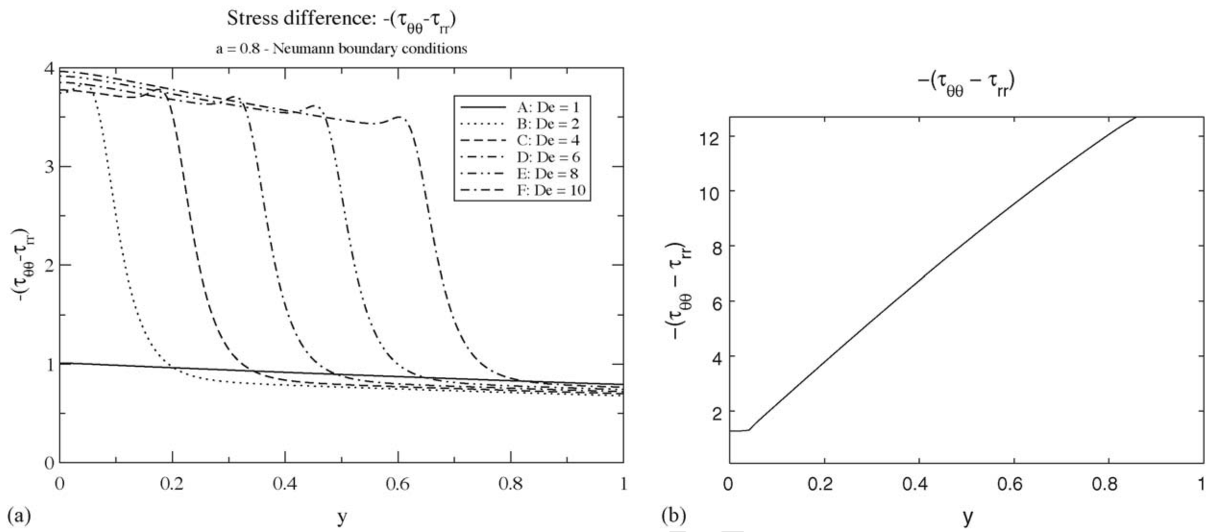

Fig. 8. In (a), radial variations in the first normal stress difference are plotted for different values of the apparent shear rate following the left ascending stable branch and then the lower plateau as indicated in Fig. 6. At right, (b) we show the spatial extent of first normal stress difference contour for $N_1 = 3$ as Deborah number is increased with Neumann boundary conditions on the conformation tensor.

We could not numerically resolve a clear connection between the two "plateau" curves and the left or right stable branches, and this remains a topic for further exploration.

Fig. 7 shows the velocity and number density profiles across the gap for this Neumann stress condition following the rising left curve and then the bottom plateau curve. The flow velocity curves are similar to those of Fig. 2(a) except that there is no longer a weak boundary layer at the outer cylinder. In other words these velocity profiles, with the Neumann stress conditions at the wall, following the lower branch, resemble those of Hu and Lips [17]. The number density curves, Fig. 7(b), also are quite different from those of Fig. 2(b) (Dirichlet condition). In the present case (Neumann conditions) the number density no longer depletes at the wall. Rather, the number density decreases from the inner cylinder to the outer cylinder with one localized bump/maximum at the interface of the shear bands which, in the Dirichlet condition case, moves outward as the Deborah number (inner wall velocity) increases. Fig. 8 shows the radial variations in the first normal stress difference for the Neumann stess condition. Again, there is no boundary layer at the walls in notable contrast to the Dirichlet condition case (Fig. 3). Also these curves do not show the maximum near the outer cylinder. Rather these curves show a region of high alignment and stretching near the inner wall which grows outward with increased Deborah number similar to that in Fig. 3. In addition these results show that the value of the first normal stress difference at the inner wall increases monotonically with De in contrast with results obtained using Dirichlet stress boundary conditions.

In Fig. 9, we explore values of the alignment d as we increase De moving up the left curve and onto the bottom plateau of the flow curve shown in Fig. 6. We plot the values of the alignment factor at the inner (d_i) and outer (d_o) walls as we increase De. In the Newtonian-like region of the flow curve, $De \lesssim 1.2$, the degree of alignment is equal, $d = d_o = d_i$, and d increases from zero to a value just greater than 2 as De increases. However, for $De > 1.2$, that is on the plateau, the values of the projected micellar alignment at each wall diverge so that $d_i \sim 5 \gg d_o \sim 1.8$. Thus, along the plateau this system selects a solution for which the molecules are longer and/or more highly aligned at the inner cylinder wall than at the outer cylinder wall. The separation point, and the peak in d_o, mirror the peak in the flow curve.

Along the top plateau curve in Fig. 6(a) the situation is quite different, the solutions here are close to the mirror image in y of those on the bottom curve, approximately obeying the following the symmetry:

$$n(y) \leftrightarrow n(1-y), \tag{17a}$$

$$\boldsymbol{\tau}_p(y) \leftrightarrow \boldsymbol{\tau}_p(1-y), \tag{17b}$$

$$v_\theta(y) \leftrightarrow De - v_\theta(1-y). \tag{17c}$$

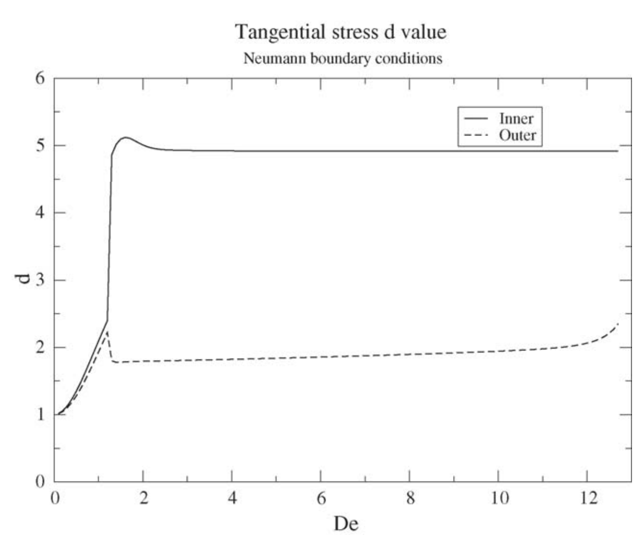

Fig. 9. Computed values of the dimensionless micellar stretch at the inner (solid) and outer (broken) walls as a function of De in shear-rate controlled flows. Solutions obtained using Neumann conformation boundary conditions.

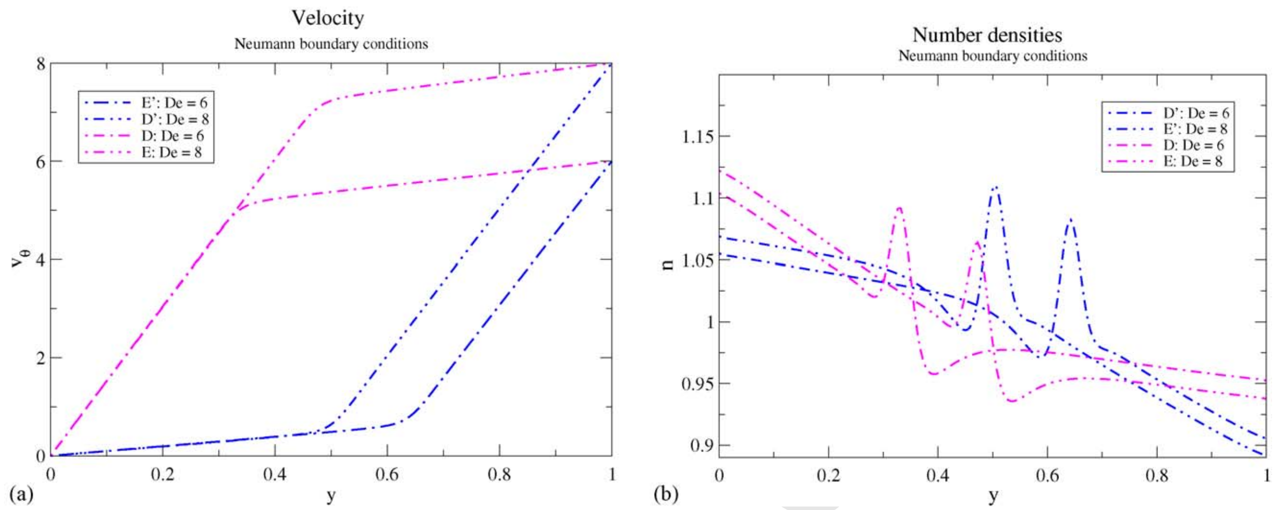

Fig. 10. A comparison of solutions along the upper and lower branch in the flow curves with Neumann stress boundary conditions. The velocity profiles are shown at left (a) at positions D/D′ and E/E′. Similarly, the number density distributions are shown at right (b).

The symmetry is approximate because it does not account for the curvilinear geometry. Thus, in contrast to the solutions on the lower branch, these solutions show a high shear-rate layer at the outer wall, a high amount of stretching/alignment at the outer wall, and a peak in number density that moves inward from near the outer wall, towards the inner wall, as *De* increases. The existence of similar transposed solutions was reported by Olmsted et al. in their study of the Taylor-Couette flow of the Johnson–Segalman model with a diffusive term [28]. We compare upper plateau and lower plateau velocities and number densities in Fig. 10. Such inverted velocity profiles have not been observed to date in velocimetry studies of worm-like micellar solutions [17,32]; however as Olmsted et al. note it may be necessary to explore specific loading/unloading protocols to access such solution structures, and furthermore they may be metastable with long diffusive transients. We have not been able to resolve numerically the steady solutions and the branch structure in the region s and s′ of Fig. 6(a), but we shall see in the next section that we can still understand the dynamics of this system without precise information on this specific part of the branch structure.

5. Stability

To calculate the (one-dimensional) linear stability of the steady solutions that are obtained along the flow curve, we consider the growth or decay of small perturbations to steady solutions:

$$n(r,t) = \bar{n}(r) + \delta\tilde{n}(r)\,\mathrm{e}^{\lambda t}, \tag{18a}$$

$$\tau_{prr}(r,t) = \bar{\tau}_{prr}(r) + \delta\tilde{\tau}_{prr}(r)\,\mathrm{e}^{\lambda t}, \tag{18b}$$

$$\tau_{p\theta\theta}(r,t) = \bar{\tau}_{p\theta\theta}(r) + \delta\tilde{\tau}_{p\theta\theta}(r)\,\mathrm{e}^{\lambda t}, \tag{18c}$$

$$\tau_{pr\theta}(r,t) = \bar{\tau}_{pr\theta}(r) + \delta\tilde{\tau}_{pr\theta}(r)\,\mathrm{e}^{\lambda t}, \tag{18d}$$

$$v(r,t) = \bar{v}(r) + \delta\tilde{v}(r)\,\mathrm{e}^{\lambda t}, \tag{18e}$$

where $\delta \ll 1$ and λ is complex. Substituting (18) into (10) and collecting all terms at order δ, we obtain the following eigenvalue/eigenfunction problem:

$$\lambda\tilde{n} = \epsilon\left[\frac{1}{r}(r\tilde{n}')' + \Xi/a\right], \tag{19a}$$

$$\begin{aligned}\lambda\tilde{\tau}_{prr} = {}& -\tilde{\tau}_{prr} - \xi\left[r\left(\frac{\bar{v}}{r}\right)'\tilde{\tau}_{pr\theta} + \bar{\tau}_{pr\theta}r\left(\frac{\tilde{v}}{r}\right)'\right] \\ &+\epsilon\left[\frac{1}{r}(r\tilde{\tau}'_{prr})' + \frac{2}{r}(\tilde{\tau}_{p\theta\theta} - \tilde{\tau}_{prr}) + \Xi\right],\end{aligned} \tag{19b}$$

$$\begin{aligned}\lambda\tilde{\tau}_{p\theta\theta} = {}& -\tilde{\tau}_{p\theta\theta} + (2-\xi)\left[r\left(\frac{\bar{v}}{r}\right)'\tilde{\tau}_{pr\theta} + \bar{\tau}_{pr\theta}r\left(\frac{\tilde{v}}{r}\right)'\right] \\ &+\epsilon\left[\frac{1}{r}(r\tilde{\tau}'_{p\theta\theta})' + \frac{2}{r}(\tilde{\tau}_{prr} - \tilde{\tau}_{p\theta\theta}) + \Xi\right],\end{aligned} \tag{19c}$$

$$\begin{aligned}\lambda\tilde{\tau}_{pr\theta} = {}& -\tilde{\tau}_{pr\theta} + \left[\bar{\tau}_{prr} - \frac{\xi}{2}(\bar{\tau}_{prr} + \bar{\tau}_{p\theta\theta})\right]r\left(\frac{\tilde{v}}{r}\right)' \\ &+\left(1-\frac{\xi}{2}\right)r\left(\frac{\bar{v}}{r}\right)'\tilde{\tau}_{prr} - \frac{\xi}{2}r\left(\frac{\bar{v}}{r}\right)'\tilde{\tau}_{p\theta\theta} \\ &+\epsilon\left[\frac{1}{r}(r\tilde{\tau}'_{pr\theta})' - \frac{4}{r}\tilde{\tau}_{pr\theta}\right] - a^2\left[\bar{n}r\left(\frac{\tilde{v}}{r}\right)' + r\left(\frac{\bar{v}}{r}\right)'\tilde{n}\right],\end{aligned} \tag{19d}$$

$$\lambda\,Re\,\tilde{v} = -\frac{1}{r^2}\left\{r^2\left[\tilde{\tau}_{pr\theta} - \beta r\left(\frac{\tilde{v}}{r}\right)'\right]\right\}', \tag{19e}$$

where

$$\begin{aligned}\Xi = \frac{1}{r}\Bigg((r\tilde{\tau}_{prr})'' - \tilde{\tau}'_{p\theta\theta} + \xi\Bigg\{r\Bigg[r\left(\frac{\bar{v}}{r}\right)'\tilde{\tau}_{pr\theta} \\ +\bar{\tau}_{pr\theta}r\left(\frac{\tilde{v}}{r}\right)'\Bigg]'\Bigg\}'\Bigg).\end{aligned} \tag{19f}$$

For the last condition, it is understood that $Re \ll 1$, so the resulting equation is integrated numerically and implicitly included in Eqs. (19a–f). From (19e), we see that

$$r\left(\frac{\tilde{v}}{r}\right)' = \frac{1}{\beta}\tilde{\tau}_{pr\theta} - \frac{C}{\beta r^2} \tag{20}$$

on $r_1 \le r \le r_1 + 1$, where C is a constant that must be determined from the boundary conditions. Solving (20) for v, we have:

$$v(r) = \frac{\tilde{v}(r_1)r}{r_1} + \frac{2C}{\beta}\left(\frac{1}{r} - \frac{r}{r_1^2}\right) + \frac{r}{\beta}\int_{r_1}^{r} \frac{\tilde{\tau}_{pr\theta}(s)}{s}\,\mathrm{d}s. \tag{21}$$

In this paper, $v(r_1)$ is always zero so the first term vanishes. We shall see later that C is a linear transformation acting on the variables $\tilde{n}$, $\tilde{\tau}_{\mathrm{p}}$ so that the problem is a classic eigensystem.

The boundary conditions for the perturbed equations in the case where the wall stress is specified (Dirichlet) are

$$\left\{ a\tilde{n}' + \frac{1}{r}(r\tilde{\tau}'_{prr})' - \frac{1}{r}\tilde{\tau}_{p\theta\theta} + \xi\left[r\left(\frac{\bar{v}}{r}\right)'\tilde{\tau}_{pr\theta} + \bar{\tau}_{pr\theta} r\left(\frac{\tilde{v}}{r}\right)'\right]' \right\}\Bigg|_{\mathrm{w}} = 0, \tag{22a}$$

$$(\tilde{\tau}_{prr} - a\tilde{n})|_{\mathrm{w}} = 0, \tag{22b}$$

$$[\tilde{\tau}_{p\theta\theta} - a(1-d)\tilde{n}]|_{\mathrm{w}} = 0, \tag{22c}$$

$$\tilde{\tau}_{pr\theta}|_{\mathrm{w}} = 0, \tag{22d}$$

$$\tilde{v}(r_1) = 0, \tag{22e}$$

$$\text{(strain rate controlled)} \quad \tilde{v}(R_2) = 0, \tag{22f}$$

$$\text{(stress-controlled)} \quad r\left(\frac{\tilde{v}}{r}\right)'\Bigg|_{r=R_2} = 0. \tag{22g}$$

The boundary conditions for the perturbed equations in the case where the derivative of the wall stresses are specified are

$$\left\{ a\tilde{n}' + \frac{1}{r}(r\tilde{\tau}'_{prr})' - \frac{1}{r}\tilde{\tau}_{p\theta\theta} + \xi\left[r\left(\frac{\bar{v}}{r}\right)'\tilde{\tau}_{pr\theta} + \bar{\tau}_{pr\theta} r\left(\frac{\tilde{v}}{r}\right)'\right]' \right\}\Bigg|_{\mathrm{w}} = 0, \tag{23a}$$

$$\tilde{\tau}'_{prr} - a\tilde{n}'|_{\mathrm{w}} = 0, \tag{23b}$$

$$\tilde{\tau}'_{p\theta\theta} - a\tilde{n}'|_{\mathrm{w}} = 0, \tag{23c}$$

$$\tilde{\tau}'_{pr\theta}|_{\mathrm{w}} = 0, \tag{23d}$$

$$\tilde{v}(r_1) = 0, \tag{23e}$$

$$\text{(shear-rate controlled)} \quad \tilde{v}(R_2) = 0, \tag{23f}$$

$$\text{(stress-controlled)} \quad r\left(\frac{\tilde{v}}{r}\right)' - \frac{1}{\beta}\tilde{\tau}_{pr\theta}\Bigg|_{r=R_2} = 0. \tag{23g}$$

We calculate the linear stability for both shear-rate controlled and stress-controlled boundary conditions at the outer wall. For perturbations with controlled shear-rate, we can solve for C in (20) by applying the zero velocity perturbation at R_2:

$$C = \frac{1}{2}\left(\frac{1}{r_1^2} - \frac{1}{r_2^2}\right)^{-1}\int_{r_1}^{r_2}\frac{\tilde{\tau}_{pr\theta}(s)}{s}\,\mathrm{d}s. \tag{24}$$

For perturbations with controlled stress at the outer wall, $C = 0$. In either case, C is a linear transformation acting on the perturbation number density and stress, so the resulting system (19a–d,f) and (21) is a classic eigenvalue/eigenfunction problem.

If $\tilde{x}$ is a vector representing discretized number density and stress over the domain, excluding the boundary, on $m-2$ points then we can define a $(m-2)\times m$ matrix A_{BC} which maps $\tilde{x}$ from the interior of the domain excluding the boundary values out to full domain including the boundaries. Similarly, we can discretize (19a–d,f) and (21) as a mapping from the full domain including the boundaries to the interior of the discretized domain as an $(m-2)\times m$ matrix A_{DE}. Selecting Dirichlet or Neumann stress boundary conditions or stress- or strain-rate controlled boundary conditions on the outer wall determines A_{BC} but not A_{DE}. The full discretized eigensystem is

$$\lambda\tilde{x} = A_{\mathrm{DE}}A_{\mathrm{BC}}\tilde{x}. \tag{25}$$

Next, we turn our attention to specific results from different combinations of stress boundary conditions and strain-rate or stress-controlled boundary conditions on the outer wall.

We seek to understand the evolution of the flow as a progression of steady states if the input parameter De (for shear-rate controlled) or $\tau_{r\theta}$ at the outer wall (for stress-controlled) is changed slowly. In the experimental literature, this is often termed upward and downward “sweeps.” When $\Re(\lambda)$ is negative, solutions are stable and if it is positive solutions are unstable. Therefore, we focus on points along the flow curve where $\Re(\lambda)$ changes sign. The eigenfunction corresponding to an eigenvalue with a small positive real part indicates the form of the growing disturbance to the steady solution as the system becomes unstable.

For Dirichlet boundary conditions where we specify the stress at the walls, the evolution of the spectrum of the perturbed system (19) along the plateau and at the cusp on Fig. 1(a), characterizes the transitions to instability. All transitions are saddle-node instabilities where a single pure real eigenvalue crosses from the left half-plane to the right half-plane. The structure of these instabilities along the plateau is shown for both the shear-rate controlled boundary conditions Fig. 11(a) and (b) near point G in Fig. 1(a) and stress-controlled boundary conditions Fig. 11(c) and (d) near point F in Fig. 1(b). If one were to perform a shear-rate controlled experiment, one would climb up past points A through G along the plateau at which point one would jump onto the right branch. From the right branch, one could decrease the shear-rate and traverse the right branch downward toward point I after which one would jump back to the left branch. With stress-controlled experiments, one would experience similar behavior except one would jump to the right branch from the plateau near point F.

For Neumann stress boundary conditions, we have not been able to resolve numerically the solution (using these steady-state

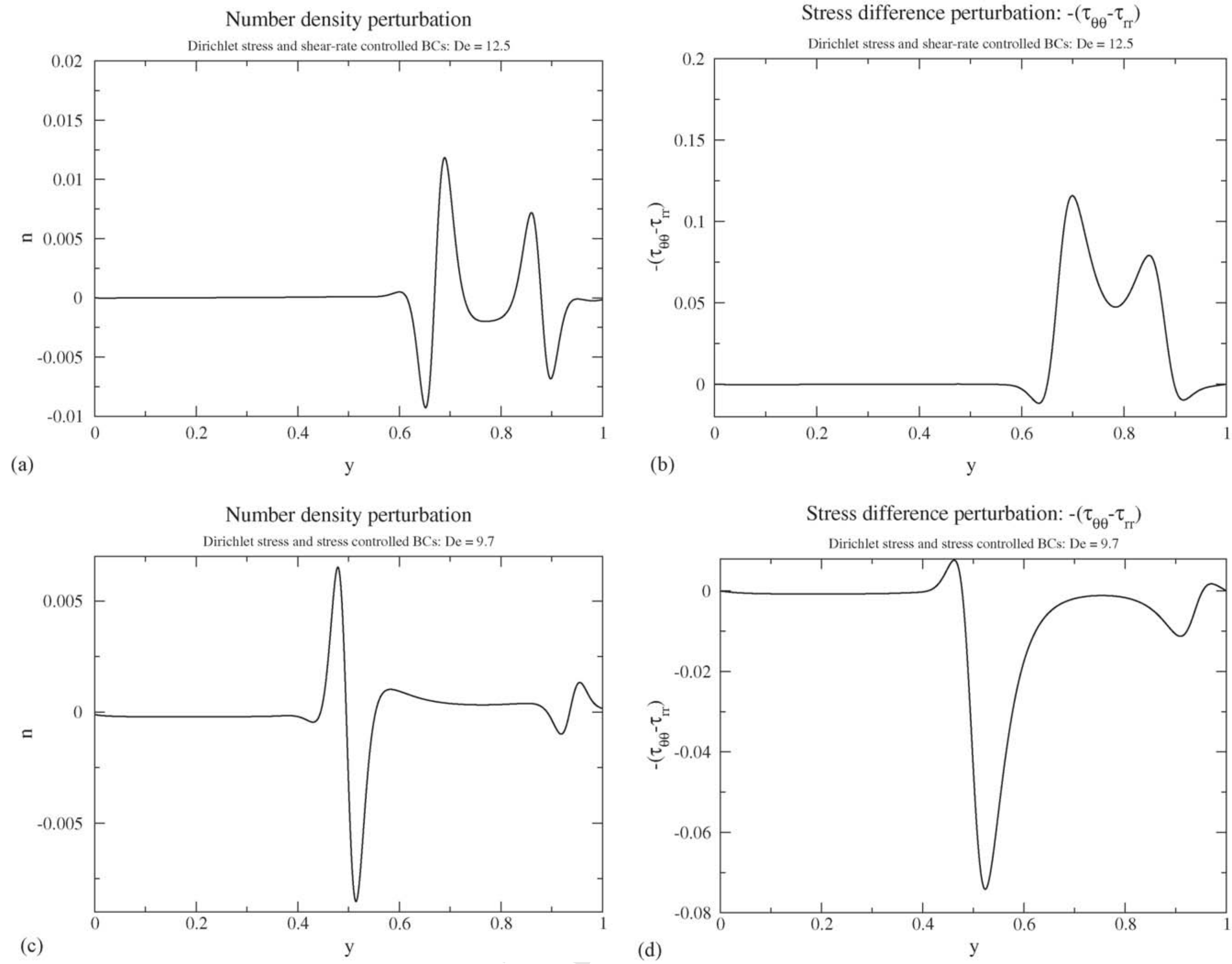

Fig. 11. Modes of instability for Dirichlet stress boundary conditions. Plots (a) and (b) are perturbations about point G in Fig. 1a. Plot (a) shows the the number density perturbation corresponding to the saddle node, and (b) shows the first normal stress difference perturbation for shear-rate controlled boundary conditions on the outer wall. Plots (c) and (d) are perturbations about point G in Fig. 1b. Similarly, plots (c) and (d) show the saddle node perturbation number density and first normal stress difference for stress-controlled boundary conditions at the outer wall.

solutions) in the region s, nor in the region s′ indicated in Fig. 6(a). The branch structure near these regions is an area for future investigation. There is a continuation branch of each of the two plateau curves towards the left (in region s), but it is unstable as indicated in the figure. In our model with Neumann stress boundary conditions, our results suggest that one will never see the middle branches with stress-controlled boundary conditions at the outer wall. One can see that the unstable perturbation shown in Fig. 12 is similar to the unsteady perturbation for the Dirichlet stress problem with stress-controlled boundary conditions (Fig. 11(c) and (d)). The key difference is that the steady solution with Dirichlet stress boundary conditions (Fig. 2) has a boundary layer at the outer wall whereas the steady solution with Neumann stress boundary conditions (Fig. 7) does not. Thus, the unstable perturbation with Dirichlet stress boundary conditions has spatial structure near the outer wall while the unstable perturbation with Neumann stress boundary conditions does not.

As the stress slowly increases one expects the system will move up the up the left branch of the flow curve shown in Fig. 6(b) to its top, then as the stress increases further jump to the right branch. As the stress is reduced from a high value, one expects to move down the right hand curve, then jump to the left, thus avoiding the plateau region. This is similar to the hysteretic behavior reported in Yesilata et al. [35]. On the other hand in a shear-rate controlled slow ramp up one would expect to move up the left curve, then jump down to the top plateau curve and move to the right across this plateau, then jump down to the right hand branch and continue moving to the right thus climbing the right hand branch. In the opposite case, as the shear rate is ramped down, one expects to come down the right hand curve to its end, then jump up to the bottom plateau curve, continue moving across and then as it ends jump up to a point near s on the left hand curve and move on down. For a specific shear-rate jump up from rest it is unclear which solution would be chosen and presumably that would depend on the complete history. Assuming the system jumps to the “nearest steady solution” the lower plateau curve would be chosen. For a specific shear-rate jump up from rest it is unclear a priori what solution would be chosen and presumably that would depend on the complete history as demonstrated by Olmsted et al. [28].

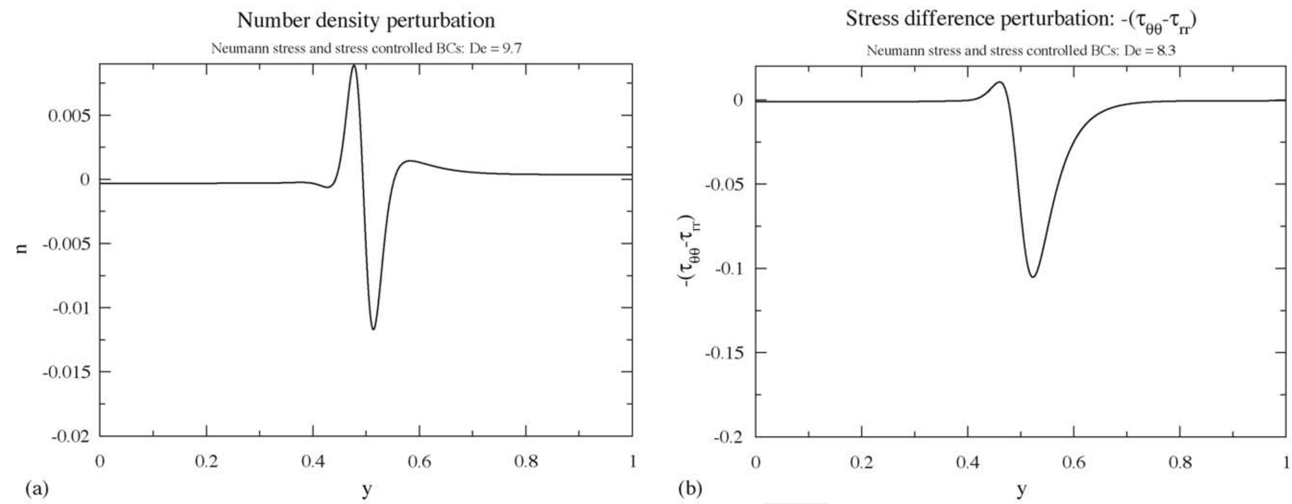

Fig. 12. Modes of instability for Neumann stress boundary conditions. Plots (a) and (b) represent perturbations about a point between E and F in Fig. 6. Plot (a) shows the the number density perturbation corresponding to the saddle node, and (b) shows the first normal stress difference perturbation with stress controlled boundary conditions at the outer wall.

6. Conclusions

In this paper, we have examined a model for dilute and semidilute unentangled worm-like micellar solutions with coupled stress and number density in axisymmetric Taylor-Couette flows. We have applied this model with parameters selected to characterize an experimental geometry that is similar to those of a number of investigators in their laboratory experiments. Calculations of the stress/strain-rate flow curve exhibit a pronounced plateau region similar to those measured in laboratory experiments. We find that coupling stress and number density provides a selection mechanism for regions in which the stress/strain-rate curve are multi-valued in agreement with our earlier results for rectilinear shear flows. However, the circular geometry reveals several notable differences. With the curvilinear geometry, the shearbands that develop in the gap are no longer symmetric about each wall. Rather, the inner boundary layer grows with apparent shear-rate until it is no longer a boundary layer but rather a full fledged shear-rate band that extends over 50% of the gap. This is an agreement with several recent particle image velocimetry experiments in worm-like micellar solutions [32,17]. At the same time, the weak outer boundary layer experiences very little change. The precise structure of the flow curve and these boundary layers depends sensitively on the choice of boundary conditions on the micellar confirmation near the walls. In the present study we have considered both Dirichlet and Neuman boundary conditions. The velocity profiles obtained using Neumann conditions Fig. 7(a) appear to be the closest to those observed experimentally.

Finally, we see regions of strong molecular alignment or stretching that originate near the inner cylinder at low apparent strain rates and propagate into the gap as the apparent strain-rate increases observation. If a critical tensile stress difference in the flow can be associated with micellar rupture and onset of turbidity then the model also captures the progressive growth of turbid regions near the rotating inner cylinder as the imposed deformation rate is increased.

Acknowledgments

This work was supported by National Science Foundation grant DMS-0405931 and DMS-0406590. Computational support was furnished via NSF SCREMS DMS-0322583. The author's thank the referees for their comments.

References

[1] V. Apostolakis, G. Mavrantzas, A.N. Beris, Stress gradient-induced migration effects in the Taylor–Couette flow of a dilute polymer solution, J. Non-Newt. Fluid Mech. 102 (2) (2002) 409–445.
[2] A.N. Beris, V.G. Mavrantzas, On the compatibility between various macroscopic formalisms for the concentration and flow of dilute polymer solutions, J. Rheol. 38 (5) (1994) 1235–1250.
[3] J.F. Berret, Transient rheology of wormlike micelles, Langmuir 13 (5) (1997) 2227–2234.
[4] J. Berret, D. Roux, G. Porte, Isotropic-to-nematic transition in wormlike micelles under shear, J. Phys. II (France) 4 (1994) 1261–1279.
[5] A.V. Bhave, R.C. Armstrong, R.A. Brown, Kinetic theory and rheology of dilute, non-homogeneous polymer solutions, J. Chem. Phys. 95 (4) (1991) 2988–3000.
[6] R.B. Bird, C.F. Curtiss, R.C. Armstrong, O. Hassager, Dynamics of Polymeric Liquids, vol. 2: Kinetic Theory, 2nd ed., John Wiley and Sons, New York, 1987.
[7] W.B. Black, M.D. Graham, Slip, concentration fluctuations, and flow instability in sheared polymer solutions, Macromolecules 34 (17) (2001) 5731–5733.
[8] M.E. Cates, Reptation of living polymers: Dynamics of entangled polymers in the prescence of reversible chain-scission reactions, Macromolecules 20 (1987) 2289–2296.
[9] L.P. Cook, L. Rossi, Shear layers and demixing in a model for shear flow of self-assembling micellar solutions, J. Non-Newt. Fluid Mech. 116 (2004) 347–369.
[10] A.W. El-Kareh, L.G. Leal, Existence of solutions for all Deborah numbers for a non-Newtonian model modified to include diffusion, J. Non-Newt. Fluid Mech. 33 (1989) 257–287.
[11] P. Espanol, X. Yuan, R. Ball, Shear banding flow in the Johnson–Segalman fluid, J. Non-Newt. Fluid Mech. 65 (1996) 93–109.
[12] S.M. Fielding, P.D. Olmsted, Early stage kinetics in a unified model of shear-induced demixing and mechanical shear banding instabilities, Phys. Rev. Lett. 90 (2003) 2240501–2240504.

[13] S.M. Fielding, P.D. Olmsted, Kinetics of shear banding instability in startup flows, Phys. Rev. E 68 (2003) 036312–036313.

[14] S.M. Fielding, P.D. Olmsted, Spatiotemporal oscillations and rheochaos in a simple model of shear banding, Phys. Rev. Lett. 9 (2004) 084502–084504.

[15] F. Greco, R. Ball, Shear-band formation in a non-Newtonian fluid model with a constitutive instability, J. Non-Newt. Fluid Mech. 69 (1997) 195–206.

[16] W. Holmes, M. López-González, P. Callaghan, Fluctuations in shear-banded flow seen by NMR velocimetry, Europhys. Lett. 64 (2) (2003) 274–280.

[17] Y.T. Hu, A. Lips, Kinetics and mechanism of shear banding in entangled micellar solutions, J. Rheol. 49 (5) (2005) 1001–1027.

[18] J. Kierzenka, L.F. Shampine, A BVP solver based on residual control and the Matlab PSE, ACM Trans. Math. Software 27 (3) (2001) 299–316.

[19] R.G. Larson, Constitutive Equations for Polymer Melts and Solutions, Butterworths, 1988.

[20] J. Lee, G. Fuller, N. Hudson, X. Yuan, Investigation of shear-banding structure in wormlike micellar solution by point-wise flow-induced birefringence measurements, J. Rheol. 49 (2) (2005) 537–550.

[21] M.W. Liberatore, F. Netlesheim, N.J. Wagner, L. Porcar, Spatially resolved SANS in the 1–2 plane: a study of shear-induced phase separating wormlike micelles, preprint.

[22] M.W. Liberatore, F. Nettlesheim, E.W. Kaler, N.J. Wagner, T. Nu, L. Porcar, Characterization of solutions of wormlike micelles underflow: Microstructure and investigations in the 1–2 plane, preprint.

[23] M.R. López-Gonzáles, W.M. Holmes, P.T. Callaghan, P.J. Photinos, Shear banding fluctuations and nematic order in wormlike micelles, Phys. Rev. Lett. 93 (2004) 2268302–2268304.

[24] C.-Y.D. Lu, P.D. Olmsted, R.C. Ball, Effects of nonlocal stress on the determination of shear banding flow, Phys. Rev. Lett. 84 (4) (2000) 642–645.

[25] V.G. Mavrantzas, A.N. Beris, Theoretical study of wall effects on rheology of dilute polymer solutions, J. Rheol. 36 (1) (1992) 175–213.

[26] J.A. Nohel, L. Pego, On the generation of discontinuous shearing motions of a non-newtonian fluid, Arch. Rational. Mech. Anal. 139 (1997) 355–376.

[27] P. Olmsted, Dynamics and flow-induced phase separation in polymeric fluids, Curr. Opinion Colloid Interface Sci. 4 (2) (1999) 95–100.

[28] P. Olmsted, O. Radulescu, C.-Y.D. Lu, Johnson–Segalman model with a diffusion term in cylindrical Couette flow, J. Rheol. 44 (2) (2000) 257–275.

[29] O. Radulescu, P.D. Olmsted, Matched asymptotic solutions for the steady banded flow of the diffusive Johnson–Segalman model in various geometries, J. Non-Newt. Fluid Mech. 91 (2000) 143–164.

[30] H. Rehage, H. Hoffmann, Viscoelastic surfactant solutions: model systems for rheological research, Mol. Phys. 74 (5) (1991) 933–973.

[31] J. Rothstein, Personal conversation, 2003.

[32] J. Salmon, A. Colin, S. Manneville, F. Molino, Velocity profiles in shear-banding wormlike micelles, Phys. Rev. Lett. 90 (22) (2003) 228303–228304.

[33] L.F. Shampine, J. Kierzenka, M.W. Reichelt, Solving boundary value problems for ordinary differential equations in Matlab with bvp4c. Technical report, The MathWorks, 2000. ftp://ftp.mathworks.com/pub/doc/papers/bvp/.

[34] E.K. Wheeler, P. Fischer, G.G. Fuller, Time-periodic flow induced structures and instabilities in a viscoelastic surfactant solution, J. Non-Newt. Fluid Mech. 75 (1998) 193–208.

[35] B. Yesilata, C. Clasen, G. McKinley, Nonlinear shear and extensional flow dynamics of wormlike surfactant solutions. JNNFM, in press.